NeuroImage 111 (2015) 590–601

Contents lists available at ScienceDirect

NeuroImage

journal homepage: www.elsevier.com/locate/ynimg

Neurite orientation dispersion and density imaging of the healthy cervical spinal cord *in vivo*

Francesco Grussu [a,*], Torben Schneider [a], Hui Zhang [b], Daniel C. Alexander [b], Claudia A.M. Wheeler–Kingshott [a]

[a] NMR Research Unit, Department of Neuroinflammation, Queen Square MS Centre, UCL Institute of Neurology, University College London, UK
[b] Department of Computer Science and Centre for Medical Image Computing, University College London, UK

ARTICLE INFO

Article history:
Accepted 24 January 2015
Available online 31 January 2015

ABSTRACT

Here we present the application of neurite orientation dispersion and density imaging (NODDI) to the healthy spinal cord *in vivo*. NODDI provides maps such as the intra-neurite tissue volume fraction (v_{in}), the orientation dispersion index (ODI) and the isotropic volume fraction (v_{iso}), and here we investigate their potential for spinal cord imaging. We scanned five healthy volunteers, four of whom twice, on a 3 T MRI system with a ZOOM-EPI sequence. In accordance to the published NODDI protocol, multiple *b*-shells were acquired at cervical level and both NODDI and diffusion tensor imaging (DTI) metrics were obtained and analysed to: i) characterise differences in grey and white matter (GM/WM); ii) assess the scan–rescan reproducibility of NODDI; iii) investigate the relationship between NODDI and DTI; and iv) compare the quality of fit of NODDI and DTI. Our results demonstrated that: i) anatomical features can be identified in NODDI maps, such as clear contrast between GM and WM in ODI; ii) the variabilities of v_{in} and ODI are comparable to that of DTI and are driven by biological differences between subjects for ODI, have similar contribution from measurement errors and biological variation for v_{in}, whereas v_{iso} shows higher variability, driven by measurement errors; iii) NODDI identifies potential sources contributing to DTI indices, as in the brain; and iv) NODDI outperforms DTI in terms of quality of fit. In conclusion, this work shows that NODDI is a useful model for *in vivo* diffusion MRI of the spinal cord, providing metrics closely related to tissue microstructure, in line with findings in the brain.

1. Introduction

Neurite orientation dispersion and density imaging (NODDI) (Zhang et al., 2012) is a model-based diffusion-weighted (DW) MRI technique that allows the quantification of specific microstructural features directly related to neuronal morphology. Unlike model-free techniques, such as diffusion spectrum imaging (DSI) (Wedeen et al., 2005) or diffusion propagator imaging (Descoteaux et al., 2011), which do not make any particular assumption about the local tissue microstructure, NODDI relies on the formulation of a geometric model that aims to capture the salient features of neuronal microarchitecture. This formulation tries to overcome the main limitation of phenomenological models, such as diffusion tensor imaging (DTI) (Basser et al., 1994), which are sensitive to changes in the local microstructure but only provide unspecific, surrogate information. NODDI parametrises the signal as a function of biophysically meaningful indices. In particular, the NODDI model assumes that water protons in neuronal tissue can be considered as belonging to three different pools: i) free water, modelling isotropic diffusion such as in areas contaminated by CSF; ii) restricted water within dispersed sticks, modelling dendrites and axons; and iii) anisotropically hindered water, modelling diffusion within glial cells, neuronal cell bodies and the extracellular environment. In the NODDI framework, DW data are acquired and parametric maps describing the properties of the compartments within which water pools diffuse are obtained fitting the model to the data. Such parametric maps represent indices such as neurite density and neurite orientation dispersion. The former estimates the fraction of axons and dendrites within tissue. The latter quantifies how parallel neurites are to each other. Low orientation dispersion is indicative of coherent organisation, since the orientation of single neurite elements does not deviate much from the mean overall orientation. On the other hand, high orientation dispersion occurs when neurites are dispersed in space and their orientations vary considerably from each other. In practice, NODDI can be performed in a clinically feasible time and it was recently applied with encouraging results to brain tumour (Wen et al., 2014), multiple sclerosis (MS) (Magnollay et al., 2014; Schneider et al., 2014), in vivo g-ratio estimation (Campbell et al., 2014), focal cortical dysplasia (Winston et al., 2014),

* Corresponding author at: Queen Square House, Queen Square, WC1N 3BG, London, UK.
E-mail address: francesco.grussu.12@ucl.ac.uk (F. Grussu).

http://dx.doi.org/10.1016/j.neuroimage.2015.01.045

neurofibromatosis (Billiet et al., 2014), neonatal encephalopathy (Lally et al., 2014) and healthy newborn brain (Kunz et al., 2014).

NODDI, originally developed for the brain, may potentially be a valuable and useful imaging technique also for spinal cord applications. Several diseases are known to alter the normal structure of the healthy spinal cord, such as MS (DeLuca et al., 2004; Lukas et al., 2013; Mottershead et al., 2003), spinal cord injury (Cohen-Adad et al., 2011; Tator and Fehlings, 1991), amyotrophic lateral sclerosis (Cohen-Adad et al., 2013; Sasaki et al., 1992) and others. Nonetheless, to date little investigation of neuronal morphology alteration in the pathological human spinal cord has been carried out *in vivo*. Although some applications of more advanced DW MRI techniques than DTI have been reported (Cohen-Adad et al., 2011; Duval et al., 2014; Farrell et al., 2008; Rangwala et al., 2013; Schneider et al., 2011), the majority of studies still rely on DTI, due to several technical challenges (Stroman et al., 2014; Wheeler-Kingshott et al., 2014). The spinal cord is a relatively small structure compared to the brain. Nonetheless, high resolution is required for precise localisation of grey and white matter (GM/WM) (Mohammadi et al., 2013). Physiological and instrumental artifacts may add undesired distortions and biases to the data (Summers et al., 2014; Verma and Cohen-Adad, 2014). Moreover, acquisitions are often made longer due to the employment of cardiac gating in order to reduce the effects of cerebrospinal fluid (CSF) pulsation and physiological noise (Wheeler-Kingshott et al., 2002a).

The practicality of NODDI and its encouraging results in brain studies make its potential application to the spinal cord appealing. For instance, neurite density estimates in WM may be employed to characterise axonal loss or to provide new insights about the pathological mechanisms underlying spinal cord atrophy in MS, which is strongly associated to clinical disability (Lukas et al., 2013). The quantification of neurite orientation dispersion may instead be of interest at the level of nerve roots or to assess the integrity of neuronal processes. Neurite orientation dispersion has been found to be a non-negligible feature at the typical voxel scale even in coherent areas such as the human corpus callosum (Budde and Annese, 2013), positively affecting the performance of DW MRI models when accounted for (Ferizi et al., 2013). Therefore, we speculate that it may be an important feature and a potential biomarker also in another organised region such as the spinal cord.

In this work, we present the first application of NODDI to the spinal cord *in vivo*. As a first exploratory step, the published NODDI diffusion encoding protocol developed for brain imaging was employed to acquire data at cervical level from five healthy volunteers, four of whom were scanned twice. Results from NODDI analysis were compared to those obtained with standard DTI, routinely employed in DW MRI studies in the spinal cord (Wheeler-Kingshott et al., 2014). We investigated: i) NODDI metrics, characterised by region-of-interest (ROI) analysis, which focussed on the differences between GM and WM; ii) the reproducibility of NODDI in GM and WM, assessed in the subjects who underwent the second scan; iii) the relationships linking NODDI and DTI indices, supported by the results from computer simulations; and iv) the goodness of fit of both NODDI and DTI models on the acquired data.

2. Materials and methods

In this section we provide a description of the NODDI model and implementation, of the *in vivo* data acquisition and of the steps followed for the analysis of the fitted metrics.

2.1. The NODDI model and implementation

NODDI consists of a multi-compartment representation of the DW MRI signal in each voxel (the NODDI signal model), and a related acquisition protocol, optimised according to the experiment design framework of Alexander (2008).

The NODDI model represents the signal in each voxel for a pulsed-gradient spin-echo (PGSE) experiment (Stejskal and Tanner, 1965) as the sum of the contribution from three non-exchanging tissue compartments (isotropic, intra and extra-neurite), and is written as:

$$A = A_0(v_{iso}A_{iso} + (1-v_{iso})(v_{in}A_{in} + (1-v_{in})A_{en})). \quad (1)$$

In Eq. (1), A_0 stands for the non-DW signal; v_{iso} and A_{iso} stand for the relaxation-weighted voxel volume fraction of the isotropic compartment, e.g. the isotropic volume fraction, and its associated signal decay; v_{in} and A_{in} stand for the intra-neurite volume fraction (namely the volume fraction of non-isotropic tissue occupied by neurites, also relaxation-weighted) and its relative signal decay; and A_{en} stands for the characteristic signal decay of the extra-neurite tissue compartment, including cell bodies (Zhang et al., 2012). Recently, v_{in} has also been referred to as neurite density index (NDI) (Billiet et al., 2014; Lally et al., 2014; Magnollay et al., 2014; Schneider et al., 2014), but here we shall consistently employ the abbreviation v_{in}, to be consistent with Eq. (1). Also, it should be noted that in the original work that introduced NODDI (Zhang et al., 2012), the intra-neurite and extra-neurite compartments were respectively named as "intracellular" and "extracellular", and that the volume fraction of the former was indicated as v_{ic}, rather than v_{in}. Here, we employ the new nomenclature since it summarises with greater precision the physical sources of the diffusion-weighted signal that the compartments account for.

2.2. In vivo data acquisition

2.2.1. Subjects

For this study, we recruited five healthy volunteers (3 females, median age 34 years, range 25–47), here referred to as subjects S1 to S5. All volunteers provided informed written consent and the experimental sessions were approved by the local research ethics committee.

2.2.2. MRI acquisition

Subjects were scanned on a 3 T Philips Achieva scanner, equipped with maximum gradient strength of 65 mT m^{-1}, employing a 16-channel neurovascular receive-only RF coil. Subjects S1 to S4 were scanned twice, with the second acquisition being performed within 8 months of the first one and consisting of the same acquisition protocol of the first scan. The acquisition protocol for all scans relied on a reduced field-of-view (FOV), cardiac gated PGSE ZOOM-EPI sequence (Symms et al., 2000; Wheeler-Kingshott et al., 2002b) with outer volume suppression (Wilm et al., 2007). A peripheral pulse oximeter was employed for monitoring the cardiac cycle and triggering cardiac gating. We implemented the diffusion encoding scheme according to the published NODDI protocol (Zhang et al., 2012), acquiring sequentially two high angular resolution diffusion imaging (HARDI) (Tuch et al., 2002) shells. The first shell consisted of thirty measurements at $b = 711$ s mm^{-2}, whereas the second shell consisted of sixty measurements at $b = 2855$ s mm^{-2}. Six non-DW measurements were also acquired, interleaved with the DW ones (three $b = 0$ images for each shell).

Scans were performed axial-oblique, i.e. perpendicular to the cord longitudinal direction, which was carefully aligned with the slice-selection direction (z) on a sagittal localiser. Twelve slices were acquired with the following parameters: TR = 4 RR repeats, TE = 65.50 ms (minimum TE achievable for a diffusion-weighting strength of $b = 2855$ s mm^{-2}), reduced FOV of 64×48 mm^2, SENSE factor of 1.5 in the anterior–posterior direction, resolution of $1 \times 1 \times 5$ mm^3, and triggering delay for cardiac gating of 150 ms. Different b-values were achieved by varying the gradient strength, while fixing $\Delta = 32.20$ms and $\delta = 20.50$ms for both shells. This corresponded to an effective diffusion time of $\tau_d = \Delta - \delta/3 = 25.37$ms. The total acquisition time, depending on subjects' heart rate, was approximately TA = 35 min, including survey scans and coil calibrations.

2.3. Pre-processing of the in vivo data

Pre-processing of the *in vivo* data was performed before running any further analysis, in order to reduce the effects of motion-related artifacts. In this work, we corrected for motion with a slice-wise linear registration, implemented using FSL FLIRT (Greve and Fischl, 2009; Jenkinson et al., 2002; Jenkinson and Smith, 2001) and described in detail in Appendix A. This approach has shown the highest benefits in DW MRI of the spinal cord (Mohammadi et al., 2013). Briefly, for each slice, the first acquired image, which was non-DW ($b = 0$), was chosen as the registration target. All following non-DW images were then registered to the target and the estimated registration transformations stored. Lastly, DW images, which were acquired in-between the $b = 0$ ones, were also warped to the target employing the transformations previously estimated, so that each DW image was warped employing the transformation of the closest preceding non-DW one.

2.4. Segmentation

For each subject and scan, whole cord segmentation was carried out on the mean $b = 0$ volume evaluated after motion correction. A semi-automatic active surface method (Horsfield et al., 2010) implemented in Jim (http://www.xinapse.com/home.php) was employed to obtain the cord outline ("cord finder" tool) and to create a binary mask (*fitting cord mask*) of the whole cord. Salient parameters adopted for the outlining were: nominal cord diameter of 8 mm, number of shape coefficients of 25, and order of longitudinal variation of 7. These parameters control the radial expansion of the surface describing the spinal cord and constrain its spatial smoothness, as described in detail elsewhere (Horsfield et al., 2010). The fitting cord mask was then eroded slice-by-slice to limit CSF contamination and cropped to the 6 central slices (*whole-cord mask*).

Afterwards, manual grey matter (GM) outlining was carried out on the average DW volume obtained according to the procedure described in Kearney et al. (2014). The GM and WM masks were obtained directly from the manually drawn outlines and were limited to voxels within the whole-cord mask.

2.5. Model fitting

The NODDI and DTI models were fitted within the fitting cord mask of all scans. The NODDI MATLAB (The MathWorks, Inc., Natick, Massachusetts, USA) Toolbox (http://nitrc.org/projects/noddi_toolbox) was employed for NODDI, whereas in-house MATLAB code was employed to fit DTI. In order to fit the NODDI model, the two diffusivities representing the diffusion coefficient of the isotropic compartment (d_{iso}) and the intrinsic diffusivity of the intra-neurite compartments ($d_{||}$) were fixed as in Zhang et al. (2012) to $d_{iso} = 3.00\mu m^2 ms^{-1}$ and $d_{||} = 1.70\mu m^2 ms^{-1}$, which are the values commonly employed in literature for the free diffusivity of water particles in CSF and neural tissue *in vivo* at body temperature. Both NODDI and DTI were fitted to the whole double-shell data set. Furthermore, DTI was also fitted to a reduced set of measurements, corresponding to the shell acquired at $b = 711$ s mm^{-2}. This was performed in order to evaluate the diffusion tensor in a regime where the contribution of non-Gaussian diffusion is small (Clark and Le Bihan, 2000; Farrell et al., 2008; Frøhlich et al., 2006). In practice, the DTI metrics obtained from the $b = 711$ s mm^{-2} shell were used to study the reproducibility and the relationship between DTI and NODDI, whereas DTI fitting performed to the whole double-shell set of measurements aimed to assess the overall goodness of fit of the model.

The fitting was carried out maximising the likelihood for a Rician noise model (Gudbjartsson and Patz, 1995) and the same objective function routines were employed to fit DTI and NODDI. The signal level at $b = 0$ was estimated as the mean of the non-DW measurements, as by default in the NODDI toolbox. Practically, the optimal parameters were estimated with a gradient descent algorithm, initialised by a grid search, which minimised the opposite of the log-likelihood. The parameter σ controlling the spread of the Rician distribution was always fixed before running the fitting and it was estimated voxel-by-voxel as the standard deviation of the non-DW measurements. In the freely available NODDI toolbox, the estimate of σ obtained as such is by default further scaled by a factor of 100, practically increasing the apparent SNR and pulling the noise model towards a Gaussian regime. However, in this work, we did not scale σ, since simulations proved that such a scaling can bias the fitted metrics if true Rician noise is added to the measurements at SNR levels of 10 or lower.

The following voxel-wise maps were obtained. For NODDI: the isotropic volume fraction (v_{iso}), the intra-neurite volume fraction (v_{in}) and the orientation dispersion index (ODI). Furthermore, we also calculated the effective volume fraction of the intra-neurite (restricted) compartment (v_r), as $v_r = (1 - v_{iso})v_{in}$, which differs substantially from v_{in} if v_{iso} is not negligible. For DTI, we evaluated fractional anisotropy (FA), axial, radial and mean diffusivity (AD, RD and MD respectively).

2.6. Analysis

Our analysis aimed to achieve four main goals:

1. characterisation of the fitted metrics;
2. investigation of the reproducibility of NODDI metrics;
3. investigation of the relationship between NODDI and DTI metrics;
4. characterisation of the quality of fit of NODDI and DTI.

2.6.1. Characterisation of the fitted metrics

We visually inspected the fitted metrics in all subjects and scans and characterised regional variation calculating the medians of each metric within each ROI (GM, WM and whole-cord). We also quantified the contrast (C) and the contrast-to-noise ratio (CNR) between GM and WM for all NODDI and DTI metrics as done in other studies (Gringel et al., 2009). We employed the relations

$$C = \frac{|\mu_{WM} - \mu_{GM}|}{\frac{1}{2}(\mu_{WM} + \mu_{GM})} \quad (2)$$

and

$$CNR = \frac{|\mu_{WM} - \mu_{GM}|}{\sqrt{\sigma^2_{WM} + \sigma^2_{GM}}}. \quad (3)$$

Above, symbols μ_{WM}, μ_{GM}, σ^2_{WM} and σ^2_{GM} respectively indicate the mean value of a metric within the WM and the GM masks, and the variance of the same metric within the WM and the GM masks. C and CNR were calculated only for the first scan of the subjects. For DTI, medians, C and CNR were calculated from the metrics derived from the $b = 711$ s mm^{-2} shell.

2.6.2. Reproducibility

The reproducibility of all NODDI metrics was investigated in GM, in WM and at whole-cord level separately, and the investigation aimed to characterise the variability of each metric within these three ROIs across subjects and scans. In particular, two main aspects were studied: i) the total variability of each metric; and ii) the within-subject and between-subject contributions (Bartlett and Frost, 2008), in order to estimate the fraction of variability respectively due to measurement errors and biological differences in the recruited cohort. The statistical analysis was performed in MATLAB and was carried out consistently for all ROIs and metrics in subjects S1 to S4.

In practice, for each ROI we calculated a percentage coefficient of variation (CV) and the intraclass correlation coefficient (ICC), as explained in Appendix B. CV relates the total variability of a metric to the

average value of the same metric observed across subjects and scans, and is expressed in percentage points. On the other hand, ICC ranges from 0 to 1 and estimates the fraction of the total variability due to biological differences between subjects. It follows that the fraction of the total variability due to measurements errors (i.e. within-subject variability) can be estimated as 1 − ICC. For comparison, the two statistics CV and ICC were also calculated for DTI indices obtained from the $b = 711$ s mm^{-2} shell.

2.6.3. Relationship between NODDI and DTI indices

We investigated the experimental relationship between NODDI metrics v_{in} and ODI, and DTI indices, with scatter plots of v_{in} and ODI, colour-coded according to the values of FA, AD, RD and MD in turn. The analysis reveals how key microstructural features such as neurite density and orientation dispersion contribute to the patterns of DTI indices in the spinal cord. We employed DTI metrics obtained from the $b = 711$ s mm^{-2} shell and we focussed on voxels with negligible isotropic volume fraction ($v_{iso} < 0.05$) to match as much as possible the assumption $v_{iso} = 0$ made to perform our simulations (in line with the underlying NODDI model hypothesis according to which the contribution of the isotropic compartment in areas not contaminated by CSF should be low).

In order to support the relationships observed *in vivo*, we also ran computer simulations and evaluated the theoretical patterns of FA, AD, RD and MD as functions of v_{in} and ODI that would be observed in a tissue perfectly matching the assumptions of the NODDI model at $b = 711$ s mm^{-2}, as described in detail in Appendix C. In practice, we sampled metrics v_{in} and ODI in a uniform grid of 64×64 values in the interval $[0.05; 0.95] \times [0.005; 0.5]$. We visually matched the results from simulations and the scatter plots of the *in vivo* data as follows. Values of v_{in} and ODI from the five subjects were quantised and mapped to the same grid employed for simulations. Then, values of DTI metrics from different voxels whose pairs (v_{in}, ODI) were mapped to the same location in the discrete grid were averaged, before colour-coding the scatter plots.

2.6.4. Quality of fit of NODDI and DTI

We investigated the quality of fit of both NODDI and DTI models on the full set of DW measurements of the five subjects (rescans omitted). The Bayesian Information Criterion (BIC) (Schwarz, 1978) was employed to compare the quality of fit of the two models, as in Ferizi et al. (2014), Ferizi et al. (2013), and Panagiotaki et al. (2012). We calculated in all voxels within the fitting mask the percentage relative difference between BIC values of NODDI and DTI, with respect to those of DTI, as

$$\delta\mathrm{BIC} = 100\frac{\mathrm{BIC}_{\mathrm{NODDI}} - \mathrm{BIC}_{\mathrm{DTI}}}{\mathrm{BIC}_{\mathrm{DTI}}} \quad (4)$$

with $\mathrm{BIC}_{\mathrm{NODDI}}$ and $\mathrm{BIC}_{\mathrm{DTI}}$ indicating respectively BIC values for NODDI and DTI.

3. Results

3.1. In vivo data acquisition

Illustrative raw images and ROIs relative to several slices of the first scan of one of the subjects (S2) are reported in Fig. 1. In the first column, the mean $b = 0$ image and the outline of the masks are shown. In the second column, DW images obtained at $b = 711$ s mm^{-2} and for a gradient direction almost perpendicular to the cord longitudinal axis are displayed. In the third column, we report DW images obtained at $b = 711$ s mm^{-2} but for a diffusion encoding gradient nearly along the cord axis. Lastly, in the fourth and fifth columns, we show DW images as in the second ad third columns but for $b = 2855$ s mm^{-2}. The first column shows that the fitting cord mask (in yellow) is likely to contain

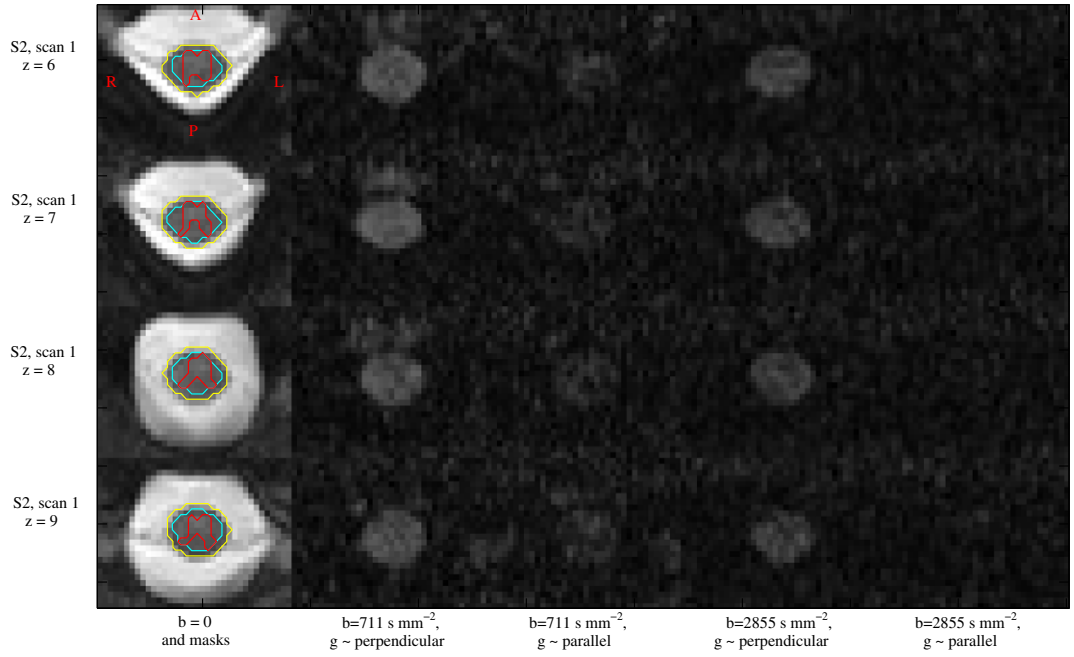

Fig. 1. Illustrative example of raw data from subject S2, first scan. Different slices are shown in different rows (slice $z = 6$ in the first row, $z = 7$ in the second, $z = 8$ in the third and $z = 9$ in the fourth, with z increasing in the inferior–superior direction). From left to right, the first column reports the mean $b = 0$ image and the contour of the fitting cord mask (yellow), of the whole-cord mask (light blue, obtained by slice-wise erosion of the yellow mask) and of the GM mask (red). The WM mask is defined as the set of voxels within the whole-cord mask which are not also within the GM mask. In the second column, the DW image obtained at $b = 711$ s mm^{-2} and for a gradient direction $\mathbf{g} = [-0.399\ 0.917\ 0.022]^{\mathrm{T}}$ (almost perpendicular to the z direction, which was carefully aligned with the cord axis on a sagittal localiser) is shown. In the third column, the DW image obtained at $b = 711$ s mm^{-2} and for a gradient direction $\mathbf{g} = [-0.049\ 0.339\ 0.940]^{\mathrm{T}}$ (almost parallel to the z direction) is shown. In the fourth column, the DW image obtained at $b = 2855$ s mm^{-2} and for a gradient direction $\mathbf{g} = [0.964\ -0.254\ 0.078]^{\mathrm{T}}$ (almost perpendicular to the z direction) is plotted. Lastly, in the fifth column, the DW image obtained at $b = 2855$ s mm^{-2} and for a gradient direction $\mathbf{g} = [0.420\ -0.533\ 0.735]^{\mathrm{T}}$ (with a high component along the z direction) is represented. Red letters R, L, A and P (top left) stand for right, left, anterior and posterior. All MRI images in the figure employ the same grey scale colour map.

voxels with CSF partial volume. Secondly, the visual inspection of the DW images reveals that diffusion weighting with gradients nearly along the cord axis causes higher attenuation than diffusion weighting with gradients almost orthogonal to the same direction. Lastly, it can be noticed that at $b = 2855$ s mm^{-2}, gradients nearly along the cord axis cause the MRI signal to decay almost completely to the noise floor.

3.2. Analysis

3.2.1. Characterisation of the fitted metrics

Fig. 2 shows illustrative voxel-wise NODDI metrics and DTI FA for a slice from both scans of subjects S2 and S3. The specific cases reported in the figure, consistent with the metrics trend observed in all subjects, show a good anatomical correspondence between scan and rescan.

The maps reveal a number of facts. Firstly, v_{iso} is maximum on the cord boundaries, where CSF partial volume is likely to occur. Moreover, although this metric is often close to 0, v_{iso} is close to 0.1 in a significant proportion of voxels. Secondly, v_{in} is close to 1 on the boundary of the fitting mask, where voxels are likely to be characterised by partial volume with CSF. In those voxels, v_{iso} is close to 1 and the effective volume fraction of the restricted compartment (v_r) is therefore very low. Also, on visual inspection, v_r shows slightly reduced contrast between GM and WM areas compared to v_{in}. Lastly, ODI shows a good contrast between GM and WM, comparable to that seen in FA maps.

Fig. 3 shows the medians of the fitted metrics within each ROI (GM, WM and whole-cord) for the five volunteers (rescans omitted), and Table 1 summarises the median and the range of these five values. Firstly, the figure confirms that v_{iso} is non-negligible on average in WM (median across the five subjects of 0.12, whereas it is 0.004 in GM). Secondly, v_{in} shows more contrast between GM and WM compared to v_r: the medians across the five subjects are 0.49 in GM and 0.57 in WM for v_{in} and 0.45 in GM 0.49 in WM for v_r. Next, the ODI contrast between GM and WM seen in Fig. 2 corresponds to values of this metric approximately three times higher in GM than in WM (median of ODI across the five volunteers of 0.086 in GM and 0.027 in WM). Lastly, Fig. 3 shows that as far as DTI metrics are concerned, FA is higher in WM compared to GM (median across the five subjects of 0.57 and 0.80 in GM and WM respectively), AD and MD are higher in WM than in GM (medians across the five subjects of 1.60μm^{2}ms^{-1} and 0.92μm^{2}ms^{-1} in GM and of 2.16μm^{2}ms^{-1} and 0.97μm^{2}ms^{-1} in WM for AD and MD respectively) and RD is higher in GM compared to WM (median across the five subjects of 0.54μm^{2}ms^{-1} in GM and 0.36μm^{2}ms^{-1} in WM).

Fig. 4 shows the contrast C and the contrast-to-noise CNR between GM and WM for the five subjects, reported as box plots. NODDI metrics v_{iso} and especially ODI provide higher values of C than DTI indices, whereas v_{in} and v_r provide similar values of such index of contrast to those of DTI MD. The CNR of NODDI metrics is comparable to that of DTI. In particular, ODI shows the highest CNR among all NODDI indices, and such value is slightly lower than the CNR of DTI FA and AD. The latter metric shows the highest CNR among all indices.

3.2.2. Reproducibility

The reproducibility analysis aims to quantify the total variability associated to the fitted metrics, and estimates how biological variation in the cohort and measurement errors contribute to this total variability. For this purpose, the indices CV (quantifying the total variability of a metric with respect to its mean across subjects and scans) and ICC (estimating the fraction of the total variability due to biological variation) were calculated and their values are reported in Tables 2 and 3.

The CV for NODDI parameters is the highest for v_{iso} (140% in GM, 41% in WM and 69% in the whole-cord ROIs) and is below 10% for v_{in} and v_r in all ROIs. Furthermore, CV for ODI is equal to 44% in GM, 7% in WM and whole-cord ROIs. The ICC is bigger than 0.5 for v_{iso} only in GM, and is just above 0.5 for v_{in} in all ROIs (ICC of 0.54, 0.62, 0.54 in GM, WM and whole-cord ROIs respectively) and it is no less than 0.66 for v_r and ODI

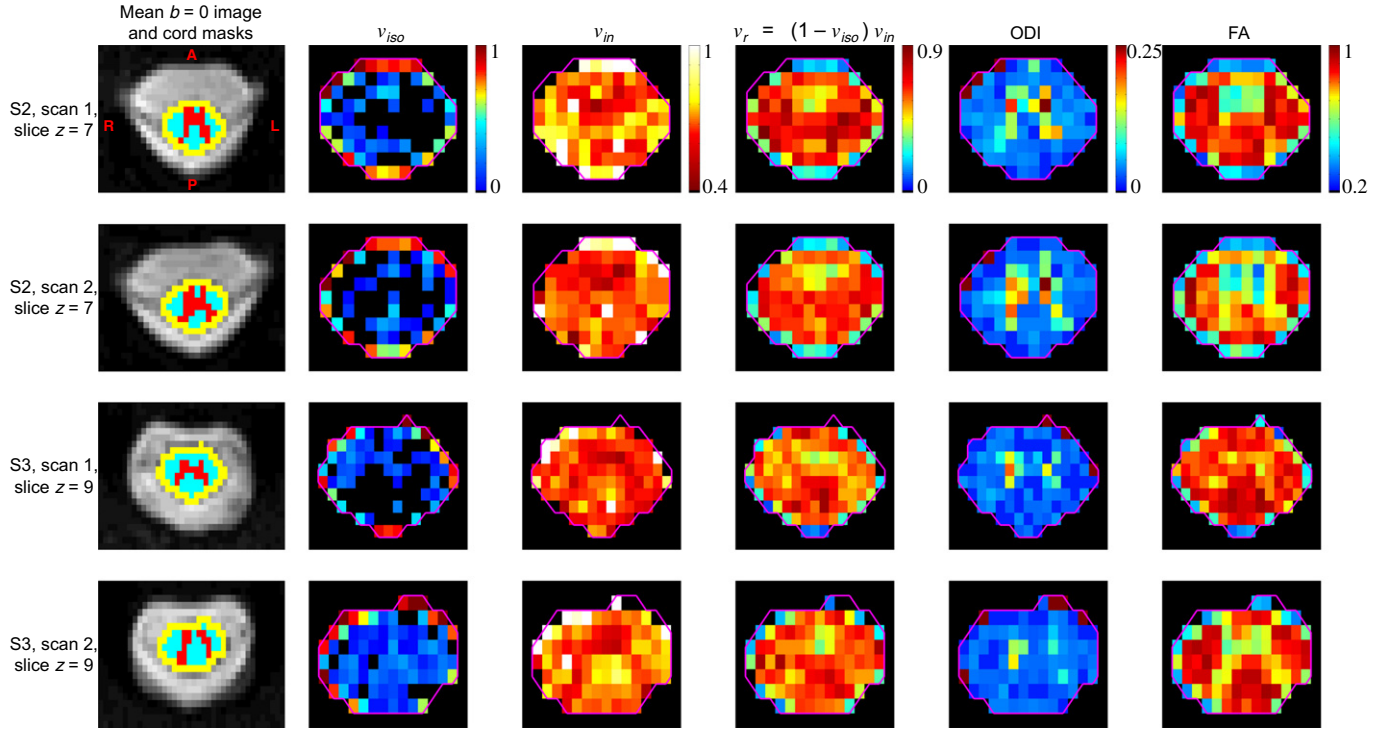

Fig. 2. Example of voxel-wise metrics for a slice from the two scans performed on subjects S2 and S3. Top to bottom: first row refers to subject S2, first scan, slice $z = 7$; second row refers to subject S2, second scan, slice $z = 7$; third row refers to subject S3, first scan, slice $z = 9$; fourth row refers to subject S3, second scan, slice $z = 9$. Left to right: first column shows the mean $b = 0$ image with overlaying fitting mask (yellow), WM mask (light blue) and GM mask (red); second column shows NODDI isotropic volume fraction (v_{iso}); third column shows NODDI intra-neurite volume fraction (v_{in}); fourth column shows NODDI effective volume fraction of the restricted compartment (v_r); fifth column shows NODDI orientation dispersion index (ODI); sixth column shows DTI fractional anisotropy (FA). Red letters R, L, A and P (top left) stand for right, left, anterior and posterior. The magenta line represents the contour of the fitting mask.

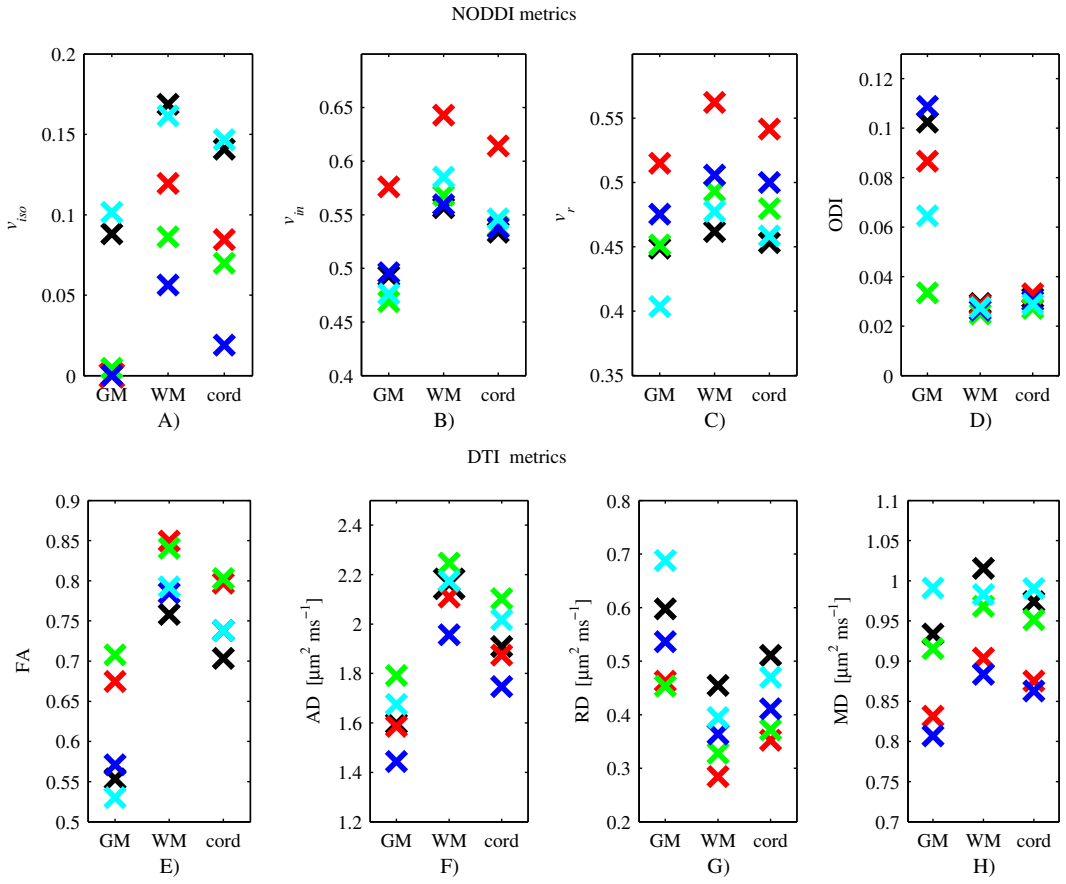

Fig. 3. Scatter plots reporting medians of NODDI and DTI metrics within all ROIs, obtained studying the first scan of all subjects. Plots in the top row refer to NODDI metrics: v_{iso} in A), v_{in} in B), v_r in C), and ODI in D). Plots in the bottom row refer to DTI metrics: FA in E); AD in F); RD in G); and MD in H). For each ROI, different markers stand for different subjects and represent the median of a metric within that particular ROI. Colours encode subjects: black stands for S1, red stands for S2, green stands for S3, blue stands for S4 and light blue stands for S5.

in all ROIs (ICC of 0.70, 0.84, 0.91 in GM, WM and whole-cord ROIs for v_r; ICC of 0.86, 0.66, 0.70 in GM, WM and whole-cord ROIs for ODI).

The CV for DTI metrics is smaller than 10% for FA in the WM and whole-cord ROIs and for AD and MD in all ROIs. CV is equal to 13% in GM for FA and it is equal to 16% in GM, 19% in WM and 17% in the whole-cord ROI for RD. Lastly, the ICC statistic is well above 0.50 for all DTI metrics in all ROIs. For instance, it was maximum for FA in GM (0.95) and minimum for FA in WM and whole-cord ROIs (0.75).

3.2.3. Relationship between NODDI and DTI indices

Fig. 5 shows the relationships between DTI metrics, evaluated at low *b*-value, and NODDI indices v_{in} and ODI, for negligible v_{iso}. We report the theoretical relationships for SNR → ∞ and for SNR = 10 respectively to the left and in the central column, whereas we plot the relationships observed *in vivo* to the right.

It is apparent from the synthetic data with SNR → ∞ that several different combinations of v_{in} and ODI, simulating different cytoarchitectures of the neural tissue, produce the same value of a DTI metric such as FA. For instance, a value of FA close to 0.80, typical of WM, can potentially be explained by a broad range of combinations of v_{in} and ODI (see Fig. 4.A), such as for $v_{in} = 0.65$ and ODI = 0.06 (relatively high neurite density but modest neurite coherence) or for $v_{in} = 0.55$ and ODI = 0.02 (lower neurite density but neurites well parallel to each other). Furthermore, an increase of FA can be independently caused by an increase in v_{in} or a decrease in ODI. Also, AD decreases with increasing ODI, and has little dependence on v_{in} for combinations of ODI and v_{in} that are likely to be measured in the spinal cord in vivo (e.g. ODI smaller than 0.25 and v_{in} greater than 0.25). As far as RD is concerned, increasing values of v_{in} imply a reduction of RD, given the lower amount of diffusion occurring in the extra-neurite compartment, whereas an increase of ODI contributes to an increased RD, if v_{in} is not too low, e.g. higher than 0.2. Lastly, MD shows little dependence on ODI in general, and decreases for increasing v_{in}, as a result of increased contribution from the restricted compartment. For completeness, it is worth noticing that the simulation suggests that DTI can underestimate the intrinsic diffusivities of the substrate if restricted diffusion dominates; this is the scenario for very high v_{in} values, which however was not observed *in vivo*.

Results from simulations at a SNR level of 10 are reported in the central plots of Fig. 4. They represent the relationship between DTI indices and metrics v_{in} and ODI that could be observed if the imaged tissue matched exactly the NODDI model assumptions and the parameters employed to run the simulations, for a SNR level plausible in the spinal cord *in vivo*. Hence, they can be considered as the ground truth, which

Table 1
Medians and ranges (within round brackets) across the five subjects of NODDI and DTI metrics for all ROIs. The medians reported here are the medians of the five data points (black, red, green, blue and light blue) shown in Fig. 3.

Median and range	GM	WM	Whole-cord
NODDI metrics:			
$\boldsymbol{v_{iso}}$	0.004 (0.10)	0.12 (0.11)	0.08 (0.13)
$\boldsymbol{v_{in}}$	0.49 (0.11)	0.57 (0.09)	0.54 (0.08)
$\boldsymbol{v_r}$	0.45 (0.11)	0.49 (0.10)	0.50 (0.09)
ODI	0.086 (0.08)	0.027 (0.003)	0.030 (0.006)
DTI metrics:			
FA	0.57 (0.18)	0.80 (0.09)	0.74 (0.10)
AD [μm^2 ms^{-1}]	1.60 (0.35)	2.16 (0.29)	1.91 (0.36)
RD [μm^2 ms^{-1}]	0.54 (0.23)	0.36 (0.17)	0.41 (0.16)
MD [μm^2 ms^{-1}]	0.92 (0.18)	0.97 (0.13)	0.95 (0.13)

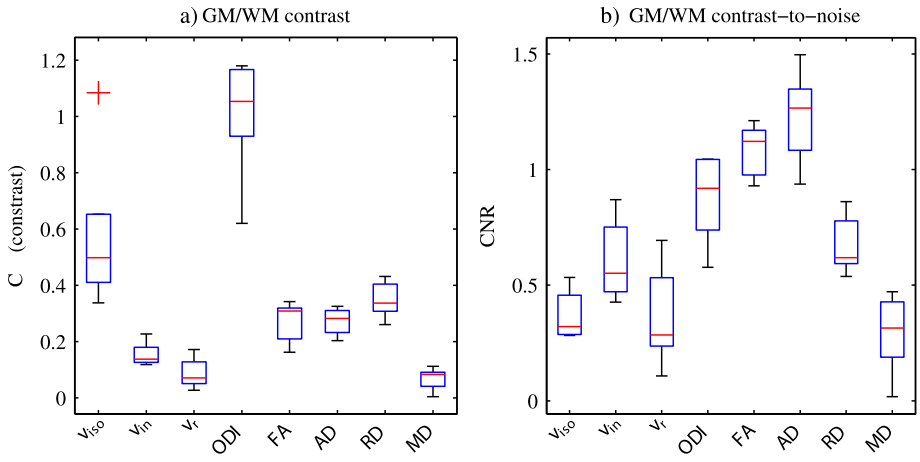

Fig. 4. To the left, in a), box plot of the contrast between GM and WM for NODDI and DTI metrics. To the right, in b), box plot of corresponding CNR values between GM and WM. The plots are obtained studying data from the first scan of all subjects, omitting rescans.

the experimental scatter plots should be compared to. The presence of Rician noise does not prevent the possibility of identifying the same general patterns seen at SNR → ∞, although contours are not as precisely delineated as before.

In vivo scatter plots, reported to the right hand side of Fig. 4, replicate the trends observed for simulations at SNR = 10 well. In the observed range, FA increases for increasing v_{in} and decreasing ODI. AD depends more on ODI rather than v_{in}, especially if the former metric is very low, and appears slightly higher than values provided by simulations. RD increases for decreasing v_{in} and for increasing ODI. Lastly, although the patterns exhibited by MD are less clear than in simulations at SNR = 10, MD decreases as v_{in} increases, especially if ODI is not too low. Also, MD appears slightly higher than the theoretical values obtained from synthetic data. Overall, *in vivo* scatter plots confirm results from simulations since the same value of all DTI metrics can be observed in voxels characterised by combinations of v_{in} and ODI considerably different to each other.

3.2.4. Quality of fit of NODDI and DTI

In this section, we report the results from the BIC analysis. BIC is a useful statistics that quantifies how well a model fits to some data while controlling for model complexity (number of model parameters), and here we employed it to compare NODDI and DTI. For this purpose, we calculated the relative percentage difference between BIC values of the NODDI and DTI models, here referred to as δBIC.

Fig. 6 shows voxel-wise δBIC maps in slices 4 to 9 of the first scan of all subjects, within the fitting mask. In Fig. 6, voxels with negative δBIC favour NODDI, positive DTI, since we always obtained positive BIC values for both models and since lower BIC implies better fitting. It is clear from the illustration that the number of voxels with negative δBIC (supporting NODDI) is overwhelmingly higher than those with positive δBIC (supporting DTI): a few voxels with δBIC > 0 are orange and yellow in slices 4, 5, 7, 8 and 9 of subject S2 and in slices 4, 5 and 6 of S5. The figure also demonstrates that voxels with extremely negative δBIC values, as low as roughly −70% (dark blue and violet voxels), are located in the cord boundary, as shown in slice 4 and 8 of subject S1, slice 4 of subject S2 or in slice 7 of subject S5. Results were consistent with other slices 1 to 3 and 10 to 12.

4. Discussion

In this work we have studied for the first time the application of NODDI to the spinal cord *in vivo*. NODDI provides metrics that map directly neurite architecture and that could potentially be important biomarkers for spinal cord conditions, and here we have shown the feasibility of applying the published technique to the healthy cervical cord *in vivo* and in a clinical setting.

Our work reveals that several known anatomical features can be identified in NODDI metrics, but also suggests that further investigation is required to better relate them to the real microstructural characteristics of the spinal cord, and in relation to other possible diffusion DW MRI models employed in brain applications, such as "ball and stick" (Behrens et al., 2003), CHARMED (Assaf et al., 2004), AxCaliber (Assaf et al., 2008) and others. The trend for our DTI indices is consistent with previous findings (Vedantam et al., 2013; Wheeler-Kingshott et al., 2002a; Xu et al., 2013) and in agreement with tract-specific measures in the lateral and dorsal columns of the cervical cord WM (Smith et al., 2010).

NODDI ODI shows the highest contrast between GM and WM among all fitted metrics, surpassing DTI indices. ODI in GM is roughly three times bigger than in WM, reflecting known existing differences

Table 2
Coefficient of variation (CV) for NODDI and DTI metrics in GM, WM and whole-cord ROIs. Values of CV smaller than 10% are shadowed in grey and displayed in bold.

CV [%]	GM	WM	Whole-cord
NODDI metrics:			
v_{iso}	140	41	69
v_{in}	**9**	**6**	**6**
v_r	**9**	**7**	**7**
ODI	44	**7**	**7**
DTI metrics:			
FA	13	**5**	**6**
AD	**9**	**7**	**8**
RD	16	19	17
MD	**8**	**7**	**7**

Table 3
Intraclass correlation coefficient (ICC) for NODDI and DTI metrics in GM, WM and whole-cord ROIs. Values of ICC bigger than 0.50 are shadowed in grey and displayed in bold.

ICC	GM	WM	Whole-cord
NODDI metrics:			
v_{iso}	**0.63**	0.33	0.41
v_{in}	**0.54**	**0.62**	**0.54**
v_r	**0.70**	**0.84**	**0.91**
ODI	**0.86**	**0.66**	**0.70**
DTI metrics:			
FA	**0.95**	**0.75**	**0.75**
AD	**0.87**	**0.77**	**0.84**
RD	**0.88**	**0.76**	**0.82**
MD	**0.81**	**0.84**	**0.88**

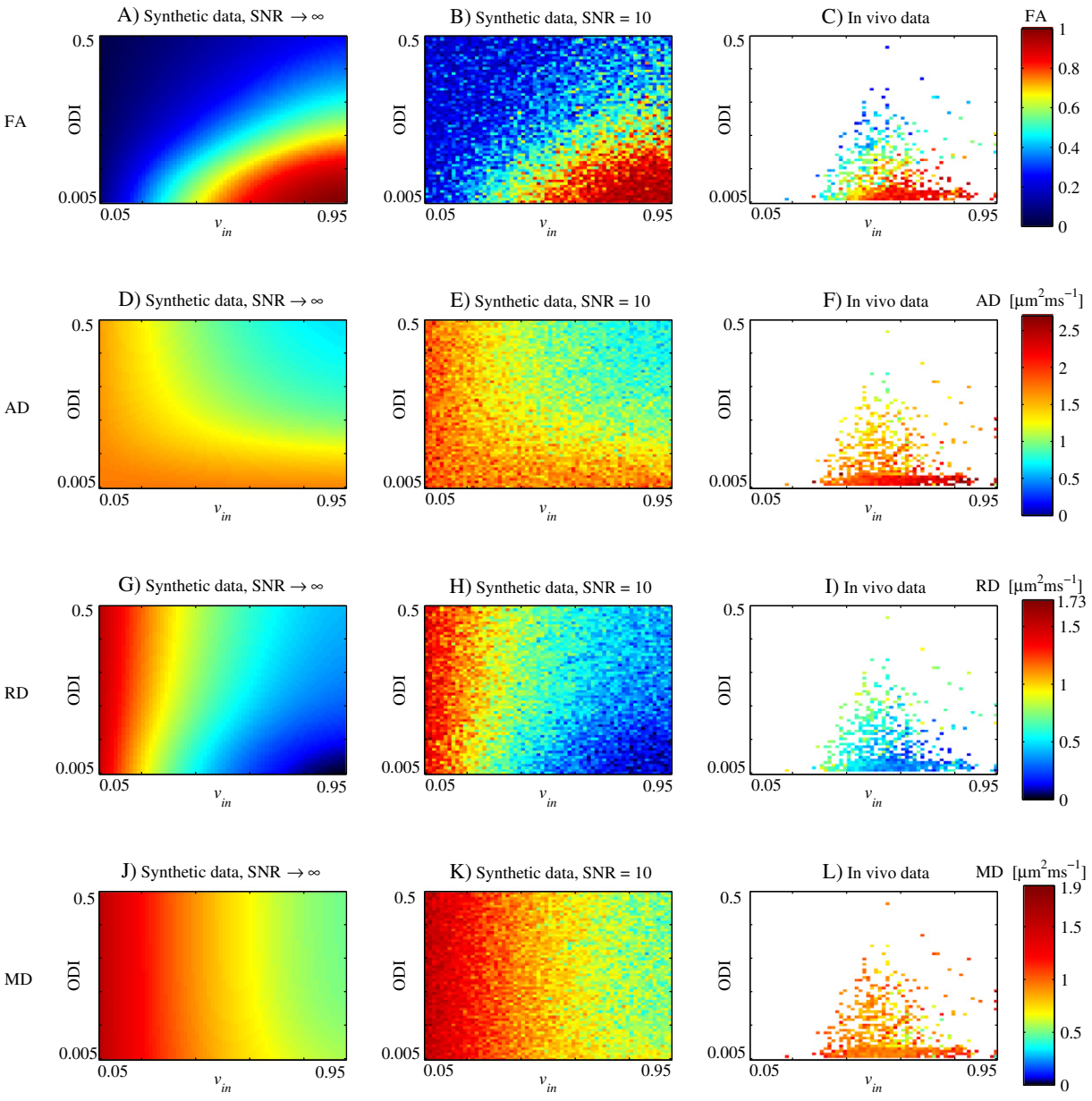

Fig. 5. Relationships between DTI metrics and NODDI indices v_{in} and ODI. Top to bottom: information about FA is reported in the first row, from A) to C); about AD in the second row, from D) to F); about RD in the third row, from G) to I); about MD in the fourth row, from J) to L). Theoretical relationships obtained from computer simulations for SNR → ∞ are shown to the left hand side, in A), D), G) and J); theoretical relationships obtained from computer simulations for SNR = 10 are shown in the central column, in B), E), H) and K); scatter plot (v_{in}, ODI) colour-coded by FA, AD, RD and MD from *in vivo* data are shown to the right hand side, in C), F), I) and L). For computer simulations, the following parameters of the NODDI signal model were fixed: $A_0 = 1$, $v_{iso} = 0$, $d_{||} = 1.70$ μm^2 ms^{-1} and $\boldsymbol{\mu} = [0\ 0\ 1]^T$. The *b*-value was fixed to $b = 711$ s mm^{-2}. The *in vivo* scatter plots were instead obtained omitting rescans and studying voxels within the whole-cord mask of subjects S1 to S5 where $v_{iso} < 0.05$. DTI metrics used for colour-coding were obtained from the $b = 711$ s mm^{-2} shell.

between the two tissue types in terms of neurite architecture and confirming qualitative findings in the brain (Zhang et al., 2012). On the other hand, volume fractions v_{in} and v_r show less contrast between GM and WM compared to ODI, similar to that of DTI MD. Though no clear quantitative comparison between GM and WM was presented in Zhang et al. (2012), results reported here seem to suggest that in the spinal cord v_{in} and v_r are more homogeneous between GM and WM compared to the brain. This could simply be a partial volume effect due to the small number of voxels in each tissue type (GM/WM), which increases the chance of contamination of the indices. On the other hand, since v_{in} is designed to map the density of both axons (prominent in WM) and dendrites (mainly found in GM), it may be possible that the reduced contrast between the two tissue types is indicative of the presence of either axons in GM or dendrites in WM, which means a reduced heterogeneity between the two tissue types in the spinal cord compared to the brain in terms of neurite density, possibly also contributing to the relatively high FA in GM. For instance, it is known from anatomy that GM strands, separated by interwoven nerve fibres, invade the WM lateral funiculus, especially at cervical level (*formatio reticularis*). Furthermore, axons originating from white funiculi and spinal nerve roots are known to be present in spinal GM: as an example, nerve fibre bundles are found in laminae I, II and IV of the posterior grey horns.

The calculation of CNR demonstrates that the CNR levels of NODDI are similar to those of DTI. Also, although ODI has the highest contrast among all metrics, its CNR is surpassed by FA and AD. This may be an effect of the higher variability of NODDI indices compared to those of DTI, which also affects the reproducibility scores. The quantification of the

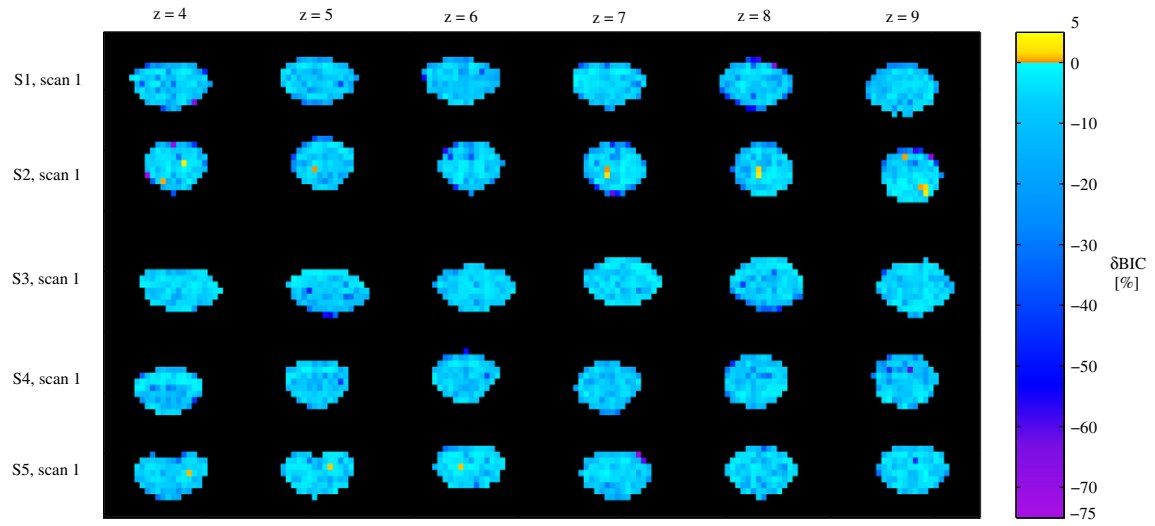

Fig. 6. Voxel-wise maps of δBIC in slices 4 to 9 of the first scan of all subjects, within the fitting mask. Slices are ordered along different columns, whereas subjects along different rows. The maps are obtained as percentage relative differences between BIC values of NODDI and DTI, choosing the BIC values of DTI as reference. Negative values correspond to voxels where the BIC of NODDI was smaller than the BIC of DTI, implying a better quality of fit of the former compared to the latter. The opposite holds for positive δBIC values.

contrast and of the CNR therefore points towards the potential of NODDI for spinal cord applications, since the technique clearly differentiates the microstructural differences of GM and WM in terms of neurite orientation dispersion. However, future optimisation of the technique for the spinal cord should help to reduce the variability of the metrics, and hence to enhance the CNR measured in this work.

Our analysis also shows that v_{iso} is maximum in the cord boundaries, where CSF contamination is likely. Potential CSF contamination is also suggested in those areas by v_{in} and v_r, which are respectively very high and very low. Moreover, when v_{iso} is very high, namely $v_{iso} \rightarrow 1$, then v_{in} is also usually high and differs considerably from v_r. However, in such cases v_{in} is poorly defined as the tissue signal is very low. We also observe that an amount of v_{iso} close to 0.1 is seen in WM. Residual CSF partial volume effects in correspondence of the anterior median fissure and the central canal may contribute in voxels within the neural tissue, but it is likely that v_{iso} explains the fraction of signal decay that can not be associated directly with restricted diffusion, i.e. relatively isotropic diffusion but slower than diffusion in CSF. We speculate that such relatively isotropic contributions to the DW signal in WM may partly arise from the water pool within the biggest axons. A tiny but non-negligible percentage of axons is known to be characterised by large diameters (Feirabend et al., 2002; Häggqvist, 1936; Wesselink et al., 1998) with the tails of the fibre diameter distribution at cervical level extending up to 15 μm and beyond (Makino et al., 1996). These axons, even if not numerous, can make a substantial contribution to the DW signal, given their large size and therefore relatively large volume fraction (Alexander et al., 2010). Since in this study we employed a diffusion time of 25.37 ms, which would imply a radial mean square diffusion displacement of $L_d = \sqrt{2D\,\tau_d} = 10.5\mu m$, assuming a value for the free diffusivity of water particles in neural tissue at body temperature of $D = 2.16\mu m^2 ms^{-1}$ (median AD in WM from Table 1), it can be hypothesised that spins diffusing within largest axons did not fully explore the boundaries of the compartment making diffusion appear relatively free. Moreover, the presence of collateral WM fibres (Lundell et al., 2011) or heterogeneity in terms of glial cell composition between GM and WM (Liuzzi and Miller, 1987) is not captured explicitly in the NODDI model, and may have had an impact on the observed patterns of the metrics. A preliminary analysis included as supplementary material suggests that collateral fibres in WM may be associated to a slight increase of isotropic volume fraction and neurite orientation dispersion, although a bigger sample size is needed for a definite conclusion. Radially oriented astrocytes, characteristic of the WM glial cell population in the spinal cord of mammals (Liuzzi and Miller, 1987), may contribute in a similar way, being their fine processes also collateral to the direction of WM fibre bundles.

The reproducibility analysis quantifies the general trend in terms of within and between-subject variability. Results suggest that metrics v_{in}, v_r and ODI are characterised by a total variability across subjects and scans of the same order of DTI metrics, whereas the total variability of v_{iso} is considerably greater. Nonetheless, the total variability of ODI is slightly higher than that of v_{in} and v_r. Moreover, the calculation of the ICC shows that the total variability is driven by different sources for v_{iso}, v_{in}, v_r and ODI. An ICC greater than 0.5 suggests that the variability due to biological differences is bigger than that of measurement errors, whereas the opposite holds if ICC is smaller than 0.5. Here, some of the metrics are characterised by ICC values much greater than 0.5, whilst in other cases ICC was well below 0.5. Biological differences are predominantly captured by v_r and ODI, whereas measurement errors dominate for v_{iso}. Similar contribution between these two sources of variability is instead seen for v_{in}. The worst reproducibility scores are observed for v_{iso}, which is not surprising given that it is in general very low, and negligible in GM (Table 1 shows that very little contribution of the isotropic compartment is seen in GM, causing v_{iso} to be poorly defined). For instance, a CV of 140% in GM, caused by a tiny median v_{iso} across subjects and scan, smaller than the total variability, suggests that big cohorts of subjects may be required to detect variations of v_{iso} caused by pathology. v_{iso} is intrinsically highly variable in the healthy GM and values ranging from 0 to about 0.1 appear all as biologically plausible. On the other hand, for all DTI indices, the total variability is always associated almost entirely to biological variation. We speculate that the higher amount of variability and dependence on measurement errors of NODDI metrics compared to DTI could be due to the fact that NODDI non-linear signal model is more susceptible to noise and to signal distortions arising from the unavoidable magnetic field inhomogeneities that hamper spinal cord MRI (Stroman et al., 2014; Summers et al., 2014; Verma and Cohen-Adad, 2014). Such distortions were likely to be different between scans and rescans, because of different shimming and cord alignment with the main field. Nonetheless, overall the analysis shows that the reproducibility of the three metrics v_{in}, v_r and ODI is sufficient to warrant future efforts to optimise the acquisition

for spinal cord tissue characteristics as well as the employment of NODDI in its current form.

Our simulations allow the visualisation of the relationships between NODDI metrics v_{in} and ODI and DTI indices, in the case of low diffusion weighting strength, i.e. in a regime where non-Gaussian contributions are small (Clark and Le Bihan, 2000; Farrell et al., 2008; Frøhlich et al., 2006). The colour-coded scatter plots presented here agree with the trends obtained at SNR = 10 and even at SNR → ∞, and show that different configurations of parameters v_{in} and ODI can potentially lead to similar values of each DTI index, hence replicating findings in the brain (Zhang et al., 2012). Therefore, as long as metrics v_{in} and ODI are believed to provide physical quantities mapping directly neurite morphology, NODDI appears to disentangle specific factors contributing to the exhibited patterns of DTI indices in the spinal cord in vivo.

The last piece of analysis aims to compare the quality of fit of NODDI and DTI. For this purpose, we compare voxel-wise BIC maps calculated for both models. The results show clearly that NODDI does fit the DW signal better than DTI in the vast majority of voxels, since the index δBIC, i.e. the percentage relative difference between BIC values of NODDI and DTI with respect to those of DTI, is positive in only a few scattered voxels. Moreover, the results reveal that voxels where NODDI outperforms DTI in terms of goodness of fit (e.g. voxels with δBIC values as negative as −70% or more) are located in the cord border, where CSF contamination is likely, thus suggesting that multi-compartment models can provide a better description of the signal in areas with elevated partial volume effects.

Despite the achievements of this work, our approach presents a number of limitations. The most significant is the fact that the diffusion encoding protocol employed for NODDI as published in (Zhang et al., 2012) is not optimised for the spinal cord. For instance, single fibre orientation optimisation approaches similar to that followed in Schneider et al. (2010) or multi-band strategies as in Wen et al. (2014) may be adopted in order to reduce dramatically the acquisition time. This would facilitate the inclusion of NODDI in studies where the scan time is limited, which at present may not be straightforward given a total acquisition time of roughly 35 min. Also, different priors for the intrinsic diffusivities in the signal model may be used. As an example, the prior $d_{iso} = 3.00\mu m^2 ms^{-1}$ for the diffusion coefficient of the isotropic compartment may not be optimal in areas where CSF flow related effects or vascular components are not negligible, such as in those portions of tissue occupied by the branches of the anterior spinal artery and vein, which pass into the anterior median fissure. In fact, in those areas an apparent diffusivity greater than that of free water at 37 °C may be needed to explain isotropic signal decay, as observed for instance in Baron and Beaulieu (2014) for the brain ventricles in a PGSE experiment with diffusion time of 40 ms. Preliminary analysis not included in this manuscript found that MD of voxels in areas within the CSF and likely to be affected by partial volume with large vessel, is on average roughly equal to $4.30\mu m^2 ms^{-1}$. Exploratory tests demonstrated that employing priors for d_{iso} bigger than $3.00\mu m^2 ms^{-1}$ and up to $4.30\mu m^2 ms^{-1}$, may help to reduce the value of fitted v_{iso}. Nevertheless, since this is the first attempt to apply the full brain NODDI protocol to the spinal cord *in vivo*, we adhered to the same diffusivity priors adopted in Zhang et al. (2012) for consistency. Another limitation of the work is that the reproducibility of DTI, as reported here, may be underestimated, since its signal model was fitted to a smaller number of measurements than NODDI and to a *b*-shell that was not acquired employing the shortest echo time achievable on the scanner at that particular *b*-value. Here, the same echo time was set for both *b*-shells to achieve the same T2-weighting for the three tissue compartments. This choice though caused the SNR of the lowest shell to be sub-optimal.

A further limitation of this study is related to the motion correction strategy. In the current implementation, motion corrupting the DW images was corrected employing transformations evaluated among non-DW images, due to the challenge of registering reliably images obtained at very high *b*-values with those obtained at $b = 0$, as reported in other spinal cord studies performed at high diffusion weighting (Farrell et al., 2008) and as evident from the observation of Fig. 1. Although in the literature registration transformations have been estimated directly for the DW volumes (Mohammadi et al., 2013; Xu et al., 2013) or at least for the mean DW volume (Cohen-Adad et al., 2011), it should be noted that in such studies the diffusion weighting strength was much lower than here: the maximum *b*-value was equal to 500 s mm^{-2} in Mohammadi et al. (2013), to 800 s mm^{-2} in Xu et al. (2013) and to 1000 s mm^{-2} in Cohen-Adad et al. (2011). Our procedure implicitly assumes that negligible motion has occurred during the acquisition of the DW volumes between two subsequent $b = 0$ ones, and visual inspection of the uncorrected and corrected data proved that this hypothesis described our data reasonably well. Nevertheless, improvements to the NODDI analysis pipeline could be achieved with a more precise modelling of the patterns of motion occurring during the acquisition of the DW images.

Lastly, the *a priori* choice for the intrinsic diffusivity of the neural tissue, i.e. $d_{||} = 1.70\mu m^2 ms^{-1}$, may not be optimal in the presence of pathological phenomena such as inflammation and degeneration. In these cases, different values for $d_{||}$ may be necessary, and data-driven approaches could be followed to estimate suitable $d_{||}$ priors, such as analysis of DTI-derived AD in WM. More complex fitting procedures relying on Markov chain Monte Carlo (MCMC) methods may also be employed, in order to fit $d_{||}$ and to obtain distributions of plausible $d_{||}$ values.

5. Conclusion

In summary, here we have studied for the first time multi-shell DW MRI data of the healthy cervical cord *in vivo* with NODDI, and related the results to those provided by routine DTI. The main achievement of this work is to demonstrate that NODDI can be applied successfully in the cord on a standard clinical system, and that the technique replicates key findings in the brain, as reported in Zhang et al. (2012). In particular, NODDI fits the acquired data better than DTI and neurite orientation dispersion differentiates clearly GM and WM appearing as a key factor determining the level of diffusion anisotropy. This result is in line with recent findings showing that fibre orientation dispersion is an important feature at the voxel scale even in highly organised areas such as the human corpus callosum (Budde and Annese, 2013; Ferizi et al., 2013). Moreover, the reproducibility of NODDI, quantified in both GM and WM, is seen to lie in a range that would allow its application in studies involving larger cohorts of subjects, since the CV is well below 10% for metrics v_{in} and v_r in all ROIs and for ODI in WM. The higher CV in GM for ODI, driven by biological differences between subjects (ICC of 0.86), implies though that NODDI may require larger sample sizes for studies where GM neurite orientation dispersion is key to the findings. In conclusion, NODDI is a feasible alternative to DTI for *in vivo* spinal cord imaging, and has major advantages in measuring indices specific to neurite morphology able to disentangle the main factors contributing to DTI-derived anisotropy. Future work is warranted to optimise the technique to account for spinal cord anatomy. For instance, single fibre direction optimisation of the acquisition may lead to a shorter diffusion-weighting protocol. Furthermore, the histological correlates of NODDI indices should be investigated to confirm the specificity of the metrics and the model assumptions in the presence of pathology, by means of analysis of DW MRI scans of *ex vivo* spinal cord samples.

Acknowledgements

This work was funded by the UCL Grand Challenges scheme, an initiative of the UCL School of Life and Medical Sciences, UCLH/UCL Biomedical Research Centre and the Specialist Biomedical Research Centres at Moorfields/UCL and Great Ormond Street/UCL. The NMR research unit is supported by a programme grant from the UK MS Society (grant 892/08) that funds the 3 T scanner. CWK, TS, DCA and HZ receive funding from the Engineering and Physical Sciences Research Council

(EPSRC) (grants EP/I027084/01, EP/G007748, EP/L022680/1). Also, the group receives generous support from the Department of Health's National Institute for Health Research Biomedical Research Centres (BRC), which funds the infrastructure (Capital Project Number R&D03/10/RAG0449). The authors are thankful to Dr Daniel R. Altmann for statistical advice and to the volunteers who took part in this study.

Appendix A

In this appendix we report the details of the motion correction strategy that was followed for the pre-processing of all scans. Recall that each data set consisted of two b-shells, which were acquired sequentially, with DW measurements in-between the acquisition of two $b = 0$. Let $n = 1,\ldots, 6$ be the index of the n-th $b = 0$ volume. Our motion correction aimed to realign all the acquired volumes, slice-by-slice, to the first volume of the whole acquisition, which was always non-DW (that is $b = 0$ volume $n = 1$). Let us define x, y and z as the subjects' right–left, posterior–anterior and inferior–superior directions, such that $z = 1,\ldots, 12$ is the slice index. Motion correction was implemented as follows:

1. firstly, transformations

$$\mathbf{T}_n(z) = \begin{bmatrix} \mathbf{I} & \mathbf{p}_n(z) \\ \mathbf{0}^{\mathrm{T}} & 1 \end{bmatrix} \quad (A.1)$$

were estimated with FSL FLIRT (correlation ratio search cost) (Greve and Fischl, 2009; Jenkinson et al., 2002; Jenkinson and Smith, 2001) for each $n = 2,\ldots, 6$ and $z = 1,\ldots, 12$. $\mathbf{T}_n(z)$ represents the affine transformation registering slice z of the n-th $b = 0$ volume to the same slice of $b = 0$ volume $n = 1$, and accounts for in-plane translations with components along the x and y directions. In Eq. (A.1), $\mathbf{I}$ is the 3×3 identity matrix, $\mathbf{p}_n(z) = [\delta x_n(z) \quad \delta y_n(z) \quad 0]^{\mathrm{T}}$ is the estimated in-plane translation and $0 = [0 \quad 0 \quad 0]^{\mathrm{T}}$.
2. Secondly, transformations $\mathbf{T}_n(z)$ were applied slice-by-slice to the corresponding $b = 0$ volumes and to the DW volumes. In particular, each DW volume was warped using the transformations estimated for the closest preceding $b = 0$ one.

Appendix B

This appendix aims to show how CV and ICC statistics were calculated for each metric and each ROI in the scan-rescan reproducibility analysis. Let us denote with $m_{i,j}$ the median of a particular metric within a particular ROI (GM, WM and whole-cord) for subjects S_i with $i = 1,\ldots, 4$ and for scans $j = 1, 2$. The within-subject variability was estimated as $\sigma_w^2 = \frac{1}{4}\sum_{i=1}^{4}\left(\sum_{j=1}^{2}(m_{i,j} - \overline{m}_i)^2\right)$, whereas the between-subject variability was quantified as $\sigma_B^2 = \frac{1}{3}\sum_{i=1}^{4}(\overline{m}_i - \overline{m})^2$, with $\overline{m}_i$ and $\overline{m}$ being $\overline{m}_i = \frac{1}{2}\sum_{j=1}^{2} m_{i,j}$ and $\overline{m} = \frac{1}{4}\sum_{i=1}^{4}\overline{m}_i$. The total variability associated to the metric within the ROI was then calculated as the sum (Bartlett and Frost, 2008)

$$\sigma_{TOT}^2 = \sigma_W^2 + \sigma_B^2. \quad (B.1)$$

The percentage coefficient of variation (CV) was computed as

$$\mathrm{CV} = 100\frac{\sqrt{\sigma_{TOT}^2}}{\overline{m}}, \quad (B.2)$$

whilst the intraclass correlation coefficient (ICC) was evaluated as

$$\mathrm{ICC} = \frac{\sigma_B^2}{\sigma_{TOT}^2}. \quad (B.3)$$

Appendix C

In this appendix we describe the computer simulations run to obtain the theoretical patterns of DTI metrics FA, AD, RD and MD, which would be observed in a tissue perfectly matching the NODDI model assumptions at $b = 711$ s mm^{-2}. Firstly, we synthesised the noise-free (SNR $\rightarrow \infty$) DW signal generated by the NODDI model with the NODDI MATLAB Toolbox. We fixed parameters A_0, v_{iso}, $d_{||}$ and $\boldsymbol{\mu}$ (mean orientation of the neurite orientation distribution) to $A_0 = 1$, $v_{iso} = 0$, $d_{||} = 1.70\mu\mathrm{m}^2\mathrm{ms}^{-1}$ and $\boldsymbol{\mu} = [0 \quad 0 \quad 1]^{\mathrm{T}}$, whereas we varied parameters v_{in} and ODI in a grid of 64×64 uniform values in $[0.05; 0.95] \times [0.005; 0.5]$ respectively. The signal was synthesised employing gradient directions of the $b = 711$ s mm^{-2} shell and fixing $b = 711$ s mm^{-2}. Subsequently, Rician noise was added to the synthesised measurements (SNR $\triangleq A_0/\sigma_{noise}$ of 10, comparable to levels observed in previous studies in the spinal cord *in vivo* (Vedantam et al., 2013) and to the SNR of our data). Lastly, the DTI model was fitted to the noise-free and noisy synthetic data for all possible combinations of v_{in} and ODI, employing the same MATLAB routines used to fit the in vivo data. DTI indices FA, AD, RD and MD were then obtained and displayed as functions of v_{in} and ODI for each SNR level.

Appendix D. Supplementary data

Supplementary data to this article can be found online at http://dx.doi.org/10.1016/j.neuroimage.2015.01.045.

References

Alexander, D.C., 2008. A general framework for experiment design in diffusion MRI and its application in measuring direct tissue-microstructure features. Magn. Reson. Med. 60, 439–448.
Alexander, D.C., Hubbard, P.L., Hall, M.G., Moore, E.A., Ptito, M., Parker, G.J., Dyrby, T.B., 2010. Orientationally invariant indices of axon diameter and density from diffusion MRI. Neuroimage 52, 1374–1389.
Assaf, Y., Freidlin, R.Z., Rohde, G.K., Basser, P.J., 2004. New modeling and experimental framework to characterize hindered and restricted water diffusion in brain white matter. Magn. Reson. Med. 52, 965–978.
Assaf, Y., Blumenfeld-Katzir, T., Yovel, Y., Basser, P.J., 2008. AxCaliber: a method for measuring axon diameter distribution from diffusion MRI. Magn. Reson. Med. 59, 1347–1354.
Baron, C.A., Beaulieu, C., 2014. Oscillating Gradient Spin-Echo (OGSE) diffusion tensor imaging of the human brain. Magn. Reson. Med. 72, 726–736.
Bartlett, J., Frost, C., 2008. Reliability, repeatability and reproducibility: analysis of measurement errors in continuous variables. Ultrasound Obstet. Gynecol. 31, 466–475.
Basser, P.J., Mattiello, J., LeBihan, D., 1994. MR diffusion tensor spectroscopy and imaging. Biophys. J. 66, 259–267.
Behrens, T., Woolrich, M., Jenkinson, M., Johansen-Berg, H., Nunes, R., Clare, S., Matthews, P., Brady, J., Smith, S., 2003. Characterization and propagation of uncertainty in diffusion-weighted MR imaging. Magn. Reson. Med. 50, 1077–1088.
Billiet, T., Madler, B., D'Arco, F., Peeters, R., Deprez, S., Plasschaert, E., Leemans, A., Zhang, H., den Bergh, B.V., Vandenbulcke, M., Legius, E., Sunaert, S., Emsell, L., 2014. Characterizing the microstructural basis of "unidentified bright objects" in neurofibromatosis type 1: a combined in vivo multicomponent T2 relaxation and multi-shell diffusion MRI analysis. Neuroimage Clin 4, 649–658.
Budde, M.D., Annese, J., 2013. Quantification of anisotropy and fiber orientation in human brain histological sections. Front. Integr. Neurosci. 7, 3.
Campbell, J., Stikov, N., Dougherty, R., Pike, G., 2014. Combined NODDI and qMT for full-brain g-ratio mapping with complex subvoxel microstructure. Proc 22nd Scientific Meeting of the ISMRM, Milan, Italy, p. 0393.
Clark, C.A., Le Bihan, D., 2000. Water diffusion compartmentation and anisotropy at high b values in the human brain. Magn. Reson. Med. 44, 852–859.
Cohen-Adad, J., El Mendili, M., Lehéricy, S., Pradat, P., Blancho, S., Rossignol, S., Benali, H., 2011. Demyelination and degeneration in the injured human spinal cord detected with diffusion and magnetization transfer MRI. Neuroimage 55, 1024–1033.
Cohen-Adad, J., Mendili, M.-M.E., Morizot-Koutlidis, R., Lehéricy, S., Meininger, V., Blancho, S., Rossignol, S., Benali, H., Pradat, P.-F., 2013. Involvement of spinal sensory pathway in ALS and specificity of cord atrophy to lower motor neuron degeneration. Amyotroph. Lateral Scler. Frontotemporal Degeneration 14, 30–38.
DeLuca, G., Ebers, G., Esiri, M., 2004. Axonal loss in multiple sclerosis: a pathological survey of the corticospinal and sensory tracts. Brain 127, 1009–1018.
Descoteaux, M., Deriche, R., Le Bihan, D., Mangin, J.-F., Poupon, C., 2011. Multiple q-shell diffusion propagator imaging. Med. Image Anal. 15, 603–621.
Duval, T., McNab, J., Setsompop, K., Witzel, T., Schneider, T., Huang, S., Keil, B., Klawiter, E., Wald, L., Cohen-Adad, J., 2014. In vivo estimation of axon diameter in the human spinal cord using 300 mT/m gradients. Proc 22nd Scientific Meeting of the ISMRM, Milan, Italy, p. 0099.

Farrell, J.A., Smith, S.A., Gordon-Lipkin, E.M., Reich, D.S., Calabresi, P.A., van Zijl, P., 2008. High b-value q-space diffusion-weighted MRI of the human cervical spinal cord in vivo: feasibility and application to multiple sclerosis. Magn. Reson. Med. 59, 1079–1089.

Feirabend, H., Choufoer, H., Ploeger, S., Holsheimer, J., Van Gool, J., 2002. Morphometry of human superficial dorsal and dorsolateral column fibres: significance to spinal cord stimulation. Brain 125, 1137–1149.

Ferizi, U., Schneider, T., Tariq, M., Wheeler-Kingshott, C.A., Zhang, H., Alexander, D.C., 2013. The importance of being dispersed: a ranking of diffusion MRI models for fibre dispersion using *in vivo* human brain data. Medical Image Computing and Computer-Assisted Intervention—MICCAI 2013. Springer, pp. 74–81.

Ferizi, U., Schneider, T., Panagiotaki, E., Nedjati-Gilani, G., Zhang, H., Wheeler-Kingshott, C.A., Alexander, D.C., 2014. A ranking of diffusion MRI compartment models with in vivo human brain data. Magn. Reson. Med. 72, 1785–1792.

Frøhlich, A.F., Østergaard, L., Kiselev, V.G., 2006. Effect of impermeable boundaries on diffusion-attenuated MR signal. J. Magn. Reson. 179, 223–233.

Greve, D.N., Fischl, B., 2009. Accurate and robust brain image alignment using boundary-based registration. Neuroimage 48, 63–72.

Gringel, T., Schulz-Schaeffer, W., Elolf, E., Frölich, A., Dechent, P., Helms, G., 2009. Optimized high-resolution mapping of magnetization transfer (MT) at 3 Tesla for direct visualization of substructures of the human thalamus in clinically feasible measurement time. J. Magn. Reson. Imaging 29, 1285–1292.

Gudbjartsson, H., Patz, S., 1995. The Rician distribution of noisy MRI data. Magn. Reson. Med. 34, 910–914.

Häggqvist, G., 1936. Analyse der Faserverteilung in einem Ruckenmarkquerschnitt (Th3). Z. Mikrosk. Anat. Forsch. 39, 1–34.

Horsfield, M.A., Sala, S., Neema, M., Absinta, M., Bakshi, A., Sormani, M.P., Rocca, M.A., Bakshi, R., Filippi, M., 2010. Rapid semi-automatic segmentation of the spinal cord from magnetic resonance images: application in multiple sclerosis. Neuroimage 50, 446–455.

Jenkinson, M., Smith, S., 2001. A global optimisation method for robust affine registration of brain images. Med. Image Anal. 5, 143–156.

Jenkinson, M., Bannister, P., Brady, M., Smith, S., 2002. Improved optimization for the robust and accurate linear registration and motion correction of brain images. Neuroimage 17, 825–841.

Kearney, H., Schneider, T., Yiannakas, M.C., Altmann, D.R., Wheeler-Kingshott, C.A., Ciccarelli, O., Miller, D.H., 2014. Spinal cord grey matter abnormalities are associated with secondary progression and physical disability in multiple sclerosis. J. Neurol. Neurosurg. Psychiatry http://dx.doi.org/10.1136/jnnp-2014-308241.

Kunz, N., Zhang, H., Vasung, L., O'Brien, K.R., Assaf, Y., Lazeyras, F., Alexander, D.C., Hüppi, P.S., 2014. Assessing white matter microstructure of the newborn with multi-shell diffusion MRI and biophysical compartment models. Neuroimage 96, 288–299.

Lally, P., Zhang, H., Pauliah, S., Price, D., Bainbridge, A., Balraj, G., Cady, E., Shankaran, S., Thayyil, S., 2014. Microstructural changes in neonatal encephalopathy revealed with the neurite orientation dispersion and density imaging (NODDI) model. Arch. Dis. Child Fetal Neonatal Ed. 99 (Suppl. 1), A14.

Liuzzi, F.J., Miller, R.H., 1987. Radially oriented astrocytes in the normal adult rat spinal cord. Brain Res. 403, 385–388.

Lukas, C., Sombekke, M.H., Bellenberg, B., Hahn, H.K., Popescu, V., Bendfeldt, K., Radue, E.W., Gass, A., Borgwardt, S.J., Kappos, L., 2013. Relevance of spinal cord abnormalities to clinical disability in multiple sclerosis: MR imaging findings in a large cohort of patients. Radiology 269, 542–552.

Lundell, H., Nielsen, J.B., Ptito, M., Dyrby, T.B., 2011. Distribution of collateral fibers in the monkey cervical spinal cord detected with diffusion-weighted magnetic resonance imaging. Neuroimage 56, 923–929.

Magnollay, L., Grussu, F., Wheeler-Kingshott, C., Sethi, V., Zhang, H., Chard, D., Miller, D., Ciccarelli, O., 2014. An investigation of brain neurite density and dispersion in multiple sclerosis using single shell diffusion imaging. Proc 22nd Scientific Meeting of the ISMRM, Milan, Italy, p. 2048.

Makino, M., Mimatsu, K., Saito, H., Konishi, N., Hashizume, Y., 1996. Morphometric study of myelinated fibers in human cervical spinal cord white matter. Spine 21, 1010–1016.

Mohammadi, S., Freund, P., Feiweier, T., Curt, A., Weiskopf, N., 2013. The impact of post-processing on spinal cord diffusion tensor imaging. Neuroimage 70, 377–385.

Mottershead, J., Schmierer, K., Clemence, M., Thornton, J., Scaravilli, F., Barker, G., Tofts, P., Newcombe, J., Cuzner, M., Ordidge, R., 2003. High field MRI correlates of myelin content and axonal density in multiple sclerosis. J. Neurol. 250, 1293–1301.

Panagiotaki, E., Schneider, T., Siow, B., Hall, M.G., Lythgoe, M.F., Alexander, D.C., 2012. Compartment models of the diffusion MR signal in brain white matter: a taxonomy and comparison. Neuroimage 59, 2241–2254.

Rangwala, N.A., Hackney, D.B., Dai, W., Alsop, D.C., 2013. Diffusion restriction in the human spinal cord characterized *in vivo* with high *b*-value STEAM diffusion imaging. Neuroimage 82, 416–425.

Sasaki, S., Tsutsumi, Y., Yamane, K., Sakuma, H., Maruyama, S., 1992. Sporadic amyotrophic lateral sclerosis with extensive neurological involvement. Acta Neuropathol. 84, 211–215.

Schneider, T., Wheeler-Kingshott, C.A., Alexander, D.C., 2010. In-vivo estimates of axonal characteristics using optimized diffusion MRI protocols for single fibre orientation. Medical Image Computing and Computer-Assisted Intervention—MICCAI 2010. Springer, pp. 623–630.

Schneider, T., Ciccarelli, O., Kachramanoglou, C., Thomas, D., Wheeler-Kingshott, C., 2011. Reliability of tract-specific q-space imaging metrics in healthy spinal cord. Proc 19th Scientific Meeting of the ISMRM, Montreal, Canada, p. 0680.

Schneider, T., Brownlee, W., Zhang, H., Ciccarelli, O., Miller, D., Wheeler-Kingshott, C., 2014. Application of multi-shell NODDI in multiple sclerosis. Proc 22nd Scientific Meeting of the ISMRM, Milan, Italy, p. 0019.

Schwarz, G., 1978. Estimating the dimension of a model. Ann. Stat. 6, 461–464.

Smith, S.A., Jones, C.K., Gifford, A., Belegu, V., Chodkowski, B., Farrell, J.A., Landman, B.A., Reich, D.S., Calabresi, P.A., McDonald, J.W., van Zijl, P.C., 2010. Reproducibility of tract-specific magnetization transfer and diffusion tensor imaging in the cervical spinal cord at 3 tesla. NMR Biomed. 23, 207–217.

Stejskal, E., Tanner, J., 1965. Spin diffusion measurements: spin echoes in the presence of a time-dependent field gradient. J. Chem. Phys. 42, 288.

Stroman, P.W., Wheeler-Kingshott, C., Bacon, M., Schwab, J.M., Bosma, R., Brooks, J., Cadotte, D., Carlstedt, T., Ciccarelli, O., Cohen-Adad, J., Curt, A., Evangelou, N., Fehlings, M.G., Filippi, M., Kelley, B.J., Kollias, S., Mackay, A., Porro, C.A., Smith, S., Strittmatter, S.M., Summers, P., Tracey, I., 2014. The current state-of-the-art of spinal cord imaging: methods. Neuroimage 84, 1070–1081.

Summers, P., Bauleo, A., Favilla, S., Cretti, F., Lui, F., Porro, C., 2014. Gross structure of magnetic field inhomogeneity in the human cervical spinal cord. Proc 22nd Scientific Meeting of the ISMRM, Milan, Italy, p. 1721.

Symms, M., Wheeler-Kingshott, C., Parker, G., Barker, G., 2000. Zonally-magnified oblique multislice (ZOOM) EPI. Proc 8th scientific meeting of the ISMRM, Denver, CO, USA, p. 0160.

Tator, C.H., Fehlings, M.G., 1991. Review of the secondary injury theory of acute spinal cord trauma with emphasis on vascular mechanisms. J. Neurosurg. 75, 15–26.

Tuch, D.S., Reese, T.G., Wiegell, M.R., Makris, N., Belliveau, J.W., Wedeen, V.J., 2002. High angular resolution diffusion imaging reveals intravoxel white matter fiber heterogeneity. Magn. Reson. Med. 48, 577–582.

Vedantam, A., Jirjis, M.B., Schmit, B.D., Wang, M.C., Ulmer, J.L., Kurpad, S.N., 2013. Characterization and limitations of diffusion tensor imaging metrics in the cervical spinal cord in neurologically intact subjects. J. Magn. Reson. Imaging 38, 861–867.

Verma, T., Cohen-Adad, J., 2014. Effect of respiration on the B0 field in the human spinal cord at 3 T. Magn. Reson. Med. 72 (6), 1629–1636.

Wedeen, V.J., Hagmann, P., Tseng, W.Y.I., Reese, T.G., Weisskoff, R.M., 2005. Mapping complex tissue architecture with diffusion spectrum magnetic resonance imaging. Magn. Reson. Med. 54, 1377–1386.

Wen, Q., Kelley, D., Banerjee, S., Lupo, J., Xu, D., Hess, C., Nelson, S., 2014. Clinically feasible NODDI characterization of brain tumor in 5.5 minutes using multiband EPI at 7 T. Proc 22nd scientific meeting of the ISMRM, Milan, Italy, p. 4448.

Wesselink, W.A., Holsheimer, J., Nuttin, B., Boom, H.B., King, G.W., Gybels, J.M., de Sutter, P., 1998. Estimation of fiber diameters in the spinal dorsal columns from clinical data. IEEE Trans. Biomed. Eng. 45, 1355–1362.

Wheeler-Kingshott, C.A., Hickman, S.J., Parker, G.J., Ciccarelli, O., Symms, M.R., Miller, D.H., Barker, G.J., 2002a. Investigating cervical spinal cord structure using *axial* diffusion tensor imaging. Neuroimage 16, 93–102.

Wheeler-Kingshott, C.A., Parker, G.J., Symms, M.R., Hickman, S.J., Tofts, P.S., Miller, D.H., Barker, G.J., 2002b. ADC mapping of the human optic nerve: increased resolution, coverage, and reliability with CSF-suppressed ZOOM-EPI. Magn. Reson. Med. 47, 24–31.

Wheeler-Kingshott, C., Stroman, P., Schwab, J., Bacon, M., Bosma, R., Brooks, J., Cadotte, D., Carlstedt, T., Ciccarelli, O., Cohen-Adad, J., 2014. The current state-of-the-art of spinal cord imaging: applications. Neuroimage 84, 1082–1093.

Wilm, B., Svensson, J., Henning, A., Pruessmann, K., Boesiger, P., Kollias, S., 2007. Reduced field-of-view MRI using outer volume suppression for spinal cord diffusion imaging. Magn. Reson. Med. 57, 625–630.

Winston, G.P., Micallef, C., Symms, M.R., Alexander, D.C., Duncan, J.S., Zhang, H., 2014. Advanced diffusion imaging sequences could aid assessing patients with focal cortical dysplasia and epilepsy. Epilepsy Res. 108, 336–339.

Xu, J., Shimony, J.S., Klawiter, E.C., Snyder, A.Z., Trinkaus, K., Naismith, R.T., Benzinger, T.L., Cross, A.H., Song, S.K., 2013. Improved in vivo diffusion tensor imaging of human cervical spinal cord. Neuroimage 67, 64–76.

Zhang, H., Schneider, T., Wheeler-Kingshott, C.A., Alexander, D.C., 2012. NODDI: practical *in vivo* neurite orientation dispersion and density imaging of the human brain. Neuroimage 61, 1000–1016.